



OPEN First-Principles insights into group-V impurities and their impact on germanium detector performance

Sandip Aryal✉, Enrique R. Batista & Gaoxue Wang✉

The outstanding properties of high-purity germanium (HPGe) detectors, such as excellent energy resolution, high energy sensitivity, and a low background-to-signal ratio, make them essential and ideal candidates for detecting particle signatures in nuclear processes such as neutrino-less double beta decay ($0\nu\beta\beta$). However, the presence of defects and impurities in HPGe crystals can lead to charge trapping, which affects carrier mobility and results in significant energy resolution degradation. In this work, we employ density functional theory with a hybrid functional to study the energetics of possible point defects in Ge. Our findings indicate that group-V impurities form more readily in Ge compared to vacancy and interstitial of Ge. Unlike N dopants, which yield deep trap states, P, As, and Sb create shallow traps close to the conduction band edge of Ge. Furthermore, we predict that group-V defects can condense into defect complexes with Ge vacancies. These vacancy-impurity complexes form deep traps in Ge, similar to Ge vacancies, suggesting that both vacancies and vacancy-impurity complexes contribute to charge trapping in these detectors, thereby diminishing their performance.

Keywords American Chemical Society, LaTeX

High-purity Germanium (HPGe) detectors have proven to be the most sensitive among the current technologies for detecting the radiation and particle signatures of rare physical events in nature, such as neutrino-less double beta-decay ($0\nu\beta\beta$). These detectors offer higher energy resolution, greater energy sensitivity, and lowest background signal among all detectors currently used in search of $0\nu\beta\beta$ ^{1,2}. Observing $0\nu\beta\beta$ would confirm the Majorana nature of neutrino (i.e. neutrino is its own antiparticle), leading to the violation of Lepton number^{2,3}. In that case, it would imply that neutrinos acquire mass via an effective Majorana mass term, which is inversely proportional to $0\nu\beta\beta$ half-lives. This is consistent with the observed discovery of neutrino oscillations in atmospheric and solar neutrinos oscillation experiments, which also indicate neutrinos to have non-zero mass^{2,4–8}. The widely used candidate for parent nuclei that can undergo $0\nu\beta\beta$ is the Ge isotope ⁷⁶Ge^{2,8–10}. HPGe detectors are built from high-purity Ge crystals isotopically enriched in ⁷⁶Ge, serving both as sources and detectors of $0\nu\beta\beta$ ¹¹. These Ge crystals have a low impurity concentration $< 10^{10} \text{ cm}^{-3}$ and dislocation density $< 10^4 \text{ cm}^{-2}$ ¹². They are used in several $0\nu\beta\beta$ experiments such as GERDA^{8,9,13,14} and MAJORANA^{2,3}, and more recently in LEGEND^{10,15} collaboration, which combines efforts from the two. The LEGEND-200 collaboration aims to search for $0\nu\beta\beta$ decay in enriched ⁷⁶Ge HPGe detectors of mass 200 kg, targeting a $0\nu\beta\beta$ decay half-life of 10^{27} years^{6,10}. Likewise, LEGEND-1000 aims to develop ton-scale enriched ⁷⁶Ge HPGe detector with a half-life of $0\nu\beta\beta$ decay beyond 10^{28} years¹⁰.

Despite the technical advantages of HPGe detectors, growing crystals free from defects and impurities is close to impossible. The incoming particles and radiations interacting with Ge atoms in these detectors create charge carriers that drift towards the electrodes. In large HPGe detectors, the long drift distance that these charge carriers migrate, increases the likelihood of them being trapped by impurities. Such charge trapping affects the performance of these detectors by degrading their energy resolution¹⁶. Therefore, understanding the role of defects and impurities in crystalline Ge is crucial for optimizing the fabrication process of these detectors and improving their energy resolution by eliminating defects during manufacturing. Although a low concentration of defects is desirable for optimal performance in HPGe detectors, contamination with group-V impurities such as nitrogen (N), phosphorus (P), arsenic (As), and antimony (Sb) can occur during the manufacturing process.

Theoretical Division, Los Alamos National Laboratory, Los Alamos, NM 87545, USA. ✉email: saryal@lanl.gov; gaoxuew@lanl.gov

Furthermore, previous studies have reported that group-V impurities, along with Ge vacancies, are the most common defects in Ge^{17–29}.

In this work, we employ first-principles calculations using a hybrid functional within density functional theory (DFT) to study the formation of possible group-V defects and their complexes in Ge. A comprehensive assessment of the energetics of the point defects considered in this study reveals that group-V impurities are favorable in Ge compared to vacancy and interstitial of Ge. Unlike N, Ge vacancies, and Ge interstitials, which have charge transition levels (CTLs) far from the band edges, forming deep traps, P, As, and Sb introduce ionization levels close to the conduction band edge, resulting in shallow traps in Ge. Since these group-V impurities diffuse in Ge through their interaction with vacancies^{18–21,26,28,29}, we also investigated the formation of defect complexes in Ge. We infer from our results that the group-V impurities can form complexes with vacancies; larger complexes are found to bind strongly than the smaller ones. Furthermore, such clustering lowers their formation energy, as larger complexes of group-V impurities with Ge vacancies have lower formation energies than smaller ones. The impurity-vacancy complexes introduce CTLs far from the band edges, forming deep traps in Ge. Consequently, these defect complexes are expected to act as charge-trapping centers, potentially degrading the performance of HPGe detectors.

Computational details

First-principles calculations

We employed spin-polarized plane-wave DFT as implemented in VASP (version 6.1.2)^{30,31}, in conjunction with the open-source python package SPINNEY³², to study charged defects in Ge. The local density approximation (LDA) was used to approximate the exchange-correlation energy functional during structural relaxations. The projector augmented wave (PAW) method^{33,34} was employed to account for the interactions between valence electrons and ionic cores. To model point defects—vacancies, interstitials, and substitutional group-V dopants—we constructed a $3 \times 3 \times 3$ supercell of Ge containing 216 atoms. Structural relaxations were performed at the LDA level without any symmetry constraints until the residual force on each atom was below 0.001 eV/Å. Since the local and semi-local DFT functionals are known to underestimate the bandgap of Ge due to self-interaction errors associated with these functionals, we employed a single point hybrid functional (HSE06)^{35,36} calculations on LDA relaxed structures to study the energetics of these defects.

The HSE06 functional, which partially corrects the self-interaction errors associated with the standard DFT functionals by incorporating a fraction ($\sim 25\%$) of Hartree-Fock exchange term, is known to yield accurate electronic bandgaps and lattice constants for semiconductors^{35,36}. It is noteworthy that HSE06 lattice constant of 5.61 Å for Ge agrees very well with LDA lattice constant of 5.65 Å, within 1%, suggesting that the structural properties predicted by LDA are comparable to those from HSE06 for Ge. While the lattice parameters predicted by LDA and HSE functionals are nearly identical, the corresponding local atomic relaxations near charged defects may vary considerably. To verify the reliability of the approach used, full HSE relaxations for some of the considered defects were also performed. Calculations indicate that CTLs and formation energies determined using HSE on LDA-relaxed structures are in close agreement with those obtained from fully HSE-relaxed structures. This further justifies the use of LDA relaxed structures for single-point HSE06 calculations of these charged defects. A Monkhorst-Pack³⁷ k-point mesh of $2 \times 2 \times 2$ and a plane-wave basis set with energy cutoff of 350 eV were used in these calculations. The total energy convergence criterion during self-consistent cycle was set to 10^{-6} eV.

Formalism for defect calculations

The formation energy of a charged defect was computed using^{32,38–40}

$$\Delta E_f = E_{D,q} - E_H - \sum_i n_i \mu_i + q(\epsilon_v + E_F) + E_{\text{corr}}, \quad (1)$$

where $E_{D,q}$ is the total energy of a supercell containing defect, D, in charge state q; E_H is the energy of the pristine supercell; and n_i is the number of atoms of type i added ($n_i > 0$) or removed ($n_i < 0$) in the process of forming the defect. The chemical potential of species i , $\mu_i = \mu_i^0 + \Delta\mu_i$, describes the exchange of particles with respective reservoirs and depends on the reference chemical potential of atomic species i , μ_i^0 . Here, $\Delta\mu_i$ is any deviation from the reference state. The reference chemical potential can be computed from respective standard elemental phase using DFT. For Ge, crystalline Ge is the standard phase, yielding $\mu_{\text{Ge}}^0 = -5.68$ eV/atom. Likewise, for N, the molecular gas phase is used as reference, giving $\mu_{\text{N}}^0 = -10.49$ eV/atom. For P, As, and Sb, the reference is their respective crystalline phase. Our calculations give $\mu_{\text{P}}^0 = -6.54$ eV/atom, $\mu_{\text{As}}^0 = -5.95$ eV/atom, and $\mu_{\text{Sb}}^0 = -5.40$ eV/atom, all obtained using HSE06 functional.

In Eq. (1), ϵ_v is the valence band maximum (VBM), and E_F is electron chemical potential. E_F is confined within the bandgap of Ge, such that $0 \leq E_F \leq E_g$, where 0 is the position of VBM and E_g represents the bandgap of Ge. The position of E_F in semiconductors and insulators depends on the level of doping and presence of external fields. E_{corr} , in Eq. (1), is the correction term that takes into account of finite-size effects arising due to the use of supercells in our calculations. We used the scheme of Kumagai and Oba³⁸, as implemented in the python package SPINNEY³², to compute the finite-size corrections. The correction term can be expressed as

$$E_{\text{corr}} = -E_{\text{lat}} + q\Delta\phi, \quad (2)$$

where E_{lat} is the Madelung energy of charge density ρ_d embedded in the host material in presence of jellium background and $\Delta\phi$ is the potential alignment term³².

As a function of E_F , Eq. (1) describes a straight line with a slope corresponding to the defect's charge state q . The diagram showing the variation of formation energy of a charged defect as a function of E_F for different q is the defect diagram or charge transition level (CTL) diagram. The primary purpose of this diagram is to identify CTL, which correspond to E_F value where the formation energies of two charge states become equal. CTL can be expressed in terms of the formation energies of defects in charge states q and q' as⁴⁰

$$\epsilon(q/q') = \frac{\Delta E_f(D, q; E_F = 0) - \Delta E_f(D, q'; E_F = 0)}{q' - q}, \quad (3)$$

where $\Delta E_f(D, q, E_F = 0)$ and $\Delta E_f(D, q', E_F = 0)$ are formation energies for defects in charge state q and q' at the VBM ($E_F = 0$).

CTL indicates whether a defect behaves as shallow or deep level. Shallow traps are those whose electronic states can be approximated by the hydrogen atom model, making them readily ionized at room temperature and thereby contributing free carriers in the material. Their ionization energies lie close to the band edges, typically within a few $k_B T$ (≤ 0.1 eV) from the band edges, where k_B is the Boltzmann constant and T is the absolute temperature. Conversely, when CTL is significantly far from the band edges, it indicates a deep trap. In general, deep traps affect the charge transport and optical properties of materials by facilitating charge trapping and boosting non-radiative recombination in semiconductors and insulators.

Results and discussion

Crystalline Ge

We begin with studying the structural and electronic properties of crystalline Ge. Ge adopts diamond-like structure with an FCC lattice and space group $Fd\bar{3}m$ (No. 227). The primitive basis in this crystal structure consists of two identical Ge atoms located at $(0,0,0)$ and $(1/4, 1/4, 1/4)$, associated with each FCC lattice point⁴¹. The primitive and conventional unit cell structures of Ge are shown in Fig. S1. The computed lattice parameter for Ge at LDA level in our calculations is 5.65 Å, which agrees well with the experimental lattice constant of 5.66 Å⁴² within 0.2%. The Ge-Ge bond length in our calculations is 2.45 Å. However, LDA predicts a semi-metallic behavior for Ge due to self-interaction errors associated with pure DFT local and semi-local functionals. The hybrid functional HSE06, which corrects these inaccuracies, yields an indirect bandgap of 0.79 eV for Ge (Fig. S1) at the HSE06 relaxed lattice constant ~ 5.61 Å. The computed bandgap in this work is in close agreement with the experimental bandgap of 0.740–0.785 eV at 0 K^{20,43,44}.

Ge vacancy, Ge interstitial, and group-V substitutional dopants

Structural properties

The simulations of point defects including vacancy and interstitial of Ge, substitutional group-V dopants, and their complexes, were carried out in a large $3 \times 3 \times 3$ supercell (Fig. 1a) consisting of 216 Ge atoms. This supercell was constructed from the conventional unit cell of Ge using the LDA-relaxed lattice constant ($a \sim 5.65$ Å). Such large supercell ($a \sim 16.95$ Å) minimizes interactions between a defect and its periodic images when employing the periodic supercell approach in our calculations. In Fig. 1a, the supercell is zoomed in near the defect site (D), to clearly visualize the adjacent Ge atoms bonded to D. A vacancy in this supercell is created by removing a Ge

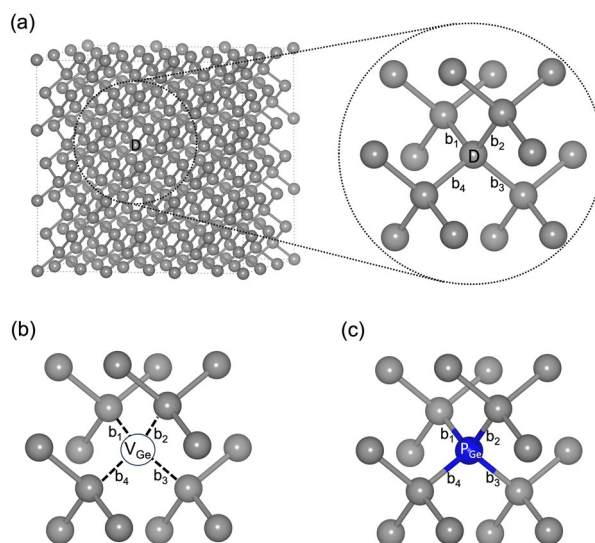


Fig. 1. (a) The 216 atoms supercell of Ge constructed from its conventional unit cell. The supercell is zoomed in near the defect site, D, to provide a clear view of the nearest Ge atoms bonded to D. In the zoomed figure, b_1 , b_2 , b_3 , and b_4 show the bond length of the Ge atom at site D with its nearest neighbors. For a pristine supercell of Ge, $b_1 = b_2 = b_3 = b_4 = 2.45$ Å, (b) Ge vacancy (V_{Ge}), and (c) P substitutional defect at D (P_{Ge}). The gray and blue spheres represent Ge and P atoms, respectively.

Defect type	V_{Ge}	P_{Ge}	N_{Ge}	As_{Ge}	Sb_{Ge}	Crystalline Ge
Bond type	V-Ge	P-Ge	N-Ge	As-Ge	Sb-Ge	Ge-Ge
Bond length	1.94 Å	2.41 Å	2.11 Å	2.49 Å	2.62 Å	2.45 Å

Table 1. Calculated defect-Ge bond lengths at LDA level. Our calculations give $b_1=b_2=b_3=b_4$ (see Fig. 1).

Method	N_{atoms}	V_{Ge}^{-2}	V_{Ge}^{-1}	V_{Ge}^0	V_{Ge}^{+1}	V_{Ge}^{+2}
LDA ⁴⁶	64	2.53	2.28	2.28	2.62	3.36
HSE ⁴⁷	64	4.03	3.38	2.87	3.34	3.98
HSE ⁴⁹	216	-	-	3.70	-	-
This work (HSE)	64	-	-	3.70	-	-
This work (HSE)	512	-	-	3.75	-	-
This work (HSE)	216	4.40	4.06	3.82	4.02	4.30

Table 2. Comparison of computed formation energy of a charged V_{Ge} with previous studies (at $E_F = 0$).

atom at site D, as shown in Fig. 1b and is labeled by V_{Ge} . Figure 1c illustrates a single Ge atom substituted by a phosphorus (P) atom, represented by P_{Ge} . Similarly, other group-V defects like Nitrogen (N), Arsenic (As), and Antimony (Sb) are labeled by N_{Ge} , As_{Ge} , and Sb_{Ge} . The defective supercells were then relaxed at LDA level of theory, which, as confirmed above, yields similar structures comparable to those obtained using HSE06. Upon relaxation, these defect supercells undergo structural changes near defect sites; however, in all cases, we found these relaxations to be short-range.

Depending on the type of defect (vacancy or substitutional) and the radius of the substituted atom, the bond distances between the defect and the nearest Ge atoms change. Table 1 summarizes the calculated defect-Ge bond lengths obtained in this work. As seen in Table 1, V_{Ge} , P_{Ge} and N_{Ge} result in bond length contraction in the vicinity of the defect site D, while the other group-V defects, As_{Ge} and Sb_{Ge} , cause the bond length elongation. The variations in defect-Ge bond lengths for different group-V defects (see Table 1) originate from the difference in their atomic radii and electronegativity. The smaller size of N and P atoms, combined with their larger electronegativity difference relative to Ge, leads to a contraction of the N-Ge and P-Ge bond lengths. Conversely, the larger atomic size of As and Sb, along with their smaller electronegativity difference with Ge, results in an elongation of the As-Ge and Sb-Ge bond lengths. Far from the defect site, Ge-Ge bond length remains unchanged, indicating that these defects only affect the local structural properties of crystalline Ge.

Formation energy and charge transition level for a Ge vacancy

Previous theoretical studies^{45–48} have investigated charged V_{Ge} using both DFT and beyond DFT methods. Table 2 presents the calculated formation energy of a charged V_{Ge} at VBM ($E_F = 0$). The computed formation energy is in reasonable agreement with previous works, considering that those works employed different levels of approximations and supercell sizes. Notably, when comparing the formation energy of V_{Ge}^0 with reported value in Ref. 49, we find excellent agreement (see Table 2). Although the formation energy of the neutral V_{Ge} calculated for the 64-atom supercell of Ge is in reasonable agreement with that of larger defect supercells, reliable CTL calculations demand greater accuracy. Furthermore, Ref. 48 reports that a supercell containing at least 216 atoms is required to achieve reliable results for a V_{Ge} . Therefore, in this study, all defect calculations were performed using a 216-atom Ge supercell.

Figure 2a illustrates the formation energy (ΔE_F) of a Ge vacancy (V_{Ge}) as a function of electron chemical potential (E_F) for various charge states: 0, ± 1 , and ± 2 . Our findings indicate that the +2 and +1 charge states of V_{Ge} exhibit higher formation energies compared to the -1, 0, and -2 charge states. Therefore, V_{Ge} if exists, is most likely to be in -1, 0, and -2 charge states, depending upon the position of E_F within the bandgap of Ge. Our calculations reveal that, among the various charge states of the V_{Ge} , V_{Ge}^{-2} is the dominant defect under n-type doping conditions, aligning with previous theoretical²⁰ and experimental¹⁷ studies. Similarly, among the various charge states of V_{Ge} and under the p-type doping conditions, V_{Ge}^0 emerges as the most stable defect, consistent with earlier theoretical research²⁰.

Figure 2 also depicts that V_{Ge} behaves as a multi-level acceptor. The computed CTLs are 0.23 eV for the -1/0 transition and 0.34 eV for the -2/-1 transition, suggesting that V_{Ge} introduces deep traps in Ge. Such deep traps are detrimental as they can lead to charge trapping, ultimately degrading the energy resolution of HPGe detectors. The obtained CTLs are shown in Fig. 2b.

The formation energy and CTLs presented in Fig. 2 were obtained from single-point HSE calculations on LDA-relaxed structures. However, full HSE relaxations can potentially produce significantly different local geometries near defects. To assess the reliability of the computed CTLs, we performed full HSE relaxations for a V_{Ge} until the residual forces on each atom were less than 0.01 eV/Å. The resulting -1/0 and -2/-1 CTLs are at 0.27 eV and 0.34 eV, respectively, for full HSE-relaxed structures, in reasonable agreement with the corresponding values of 0.23 eV and 0.34 eV obtained from single-point HSE calculations on LDA-relaxed structures. The difference is shown clearly in Fig. 3.

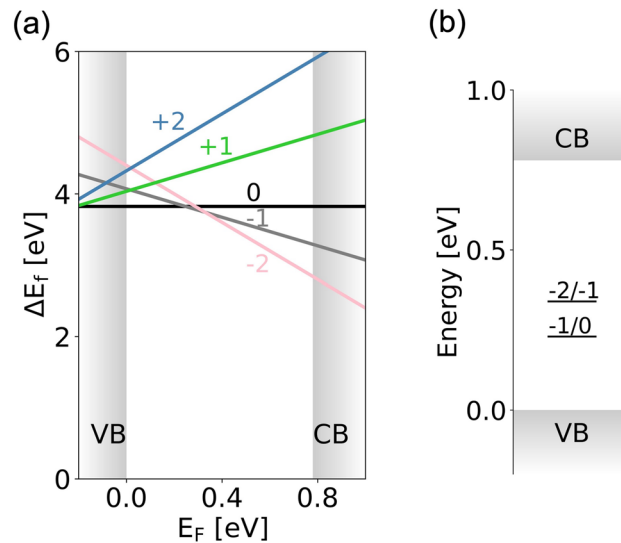


Fig. 2. (a) Formation energy (ΔE_f) as a function of the electron chemical potential (E_F) for a V_{Ge} . (b) Charge transition levels (CTLs) for a V_{Ge} . The shaded region in plots represents the valence band (VB) and conduction band (CB).

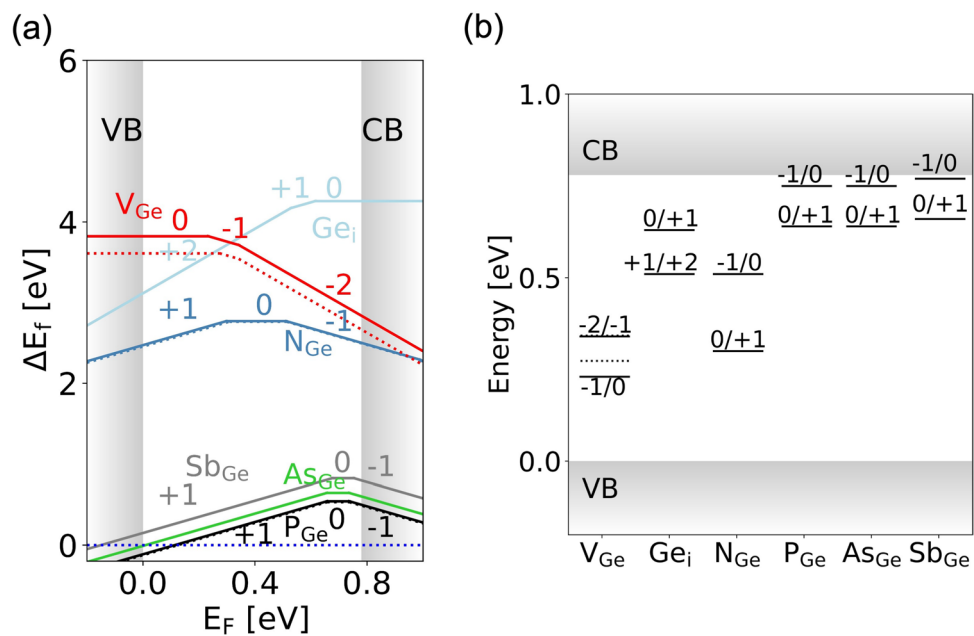


Fig. 3. (a) Formation energy (ΔE_f) as a function of the electron chemical potential (E_F) for group-V dopants in Ge. (b) Corresponding charge transition levels (CTLs) for the same dopants. For comparison, results for V_{Ge} and Ge_i are also included. The dotted lines in the plot show the corresponding results for fully relaxed HSE structures. In panel (a), P_{Ge} results obtained using full HSE-relaxed structures (dotted black lines) are shifted down by 0.01 eV to avoid overlap with solid black lines. The shaded regions denote the valence band (VB) and conduction band (CB).

Table 3 compares CTLs of a V_{Ge} obtained in this work with previous theoretical and experimental findings. The -1/0 CTL of 0.23 eV, obtained from HSE calculations on LDA-relaxed structures in this work, is in close agreement with the corresponding experimental value of 0.20 ± 0.04 eV, measured with the Perturbed Angular Correlation Spectroscopy (PAC)⁵⁰, demonstrating the reliability of our results. The -1/0 CTL obtained using fully relaxed HSE calculations is also in fair agreement with the reported experimental value.

Similarly, another experimental study utilizing Deep Level Transient Spectroscopy (DLTS) identified a transition level at 0.33 eV⁵¹ above the VBM for a V_{Ge} . Comparing our theoretical predictions with the DLTS data, we infer that the ionization level at 0.33 eV likely corresponds to -2/-1 transition for a V_{Ge} . It may be noted

Method	N_{atoms}	+1/+2	0/+1	-1/0	-2/-1
LDA ⁴⁵	128	-	0.21	0.37	0.40
GGA+U ²⁰	64	-	-	0.21	0.27
HSE ⁴⁷	64	-	-	0.50	0.65
HSE ⁴⁸	216	0.14	0.15	0.16	0.38
HSE ⁴⁹	216	-	-	-	0.33
This work (HSE @ LDA-relaxed)	216	-	-	0.23	0.34
This work (full HSE-relaxed)	216	-	-	0.27	0.34
Experiment ⁵⁰	-	-	-	0.20 ± 0.04	-

Table 3. Comparison of charge transition levels (eV) for a V_{Ge} with previous studies. “HSE @ LDA-relaxed” denotes single-point HSE calculations on LDA-relaxed structures.

that both the single-point HSE calculations on LDA-relaxed structures and full HSE-relaxed structures give -2/-1 CTL at 0.34 eV for a V_{Ge} .

The computed -2/-1 transition for a V_{Ge} in this study is in excellent agreement with the value reported in Ref. 49, which was obtained using the HSE functional with a similar supercell size and k-grid sampling. However, Ref. 49 does not report the -1/0 CTL. Another study (Ref. 48) investigated the charged V_{Ge} at the HSE level using a 216-atom Ge supercell, while the calculations are done at Γ -point. Our computed -1/0 and -2/-1 CTLs are in close agreement (within 0.05 eV) with those reported in Ref. 48. However, Ref. 48 also identifies additional 0/+1 and +1/+2 CTLs at 0.15 eV and 0.14 eV, respectively, which are not observed in our calculations. This discrepancy is due to the exclusive use of the Γ -point in their simulations. Our Γ -point calculations reproduce all the CTLs reported in Ref. 48 with +1/+2 and 0/+1 CTLs at 0.19 eV and 0.27 eV, respectively, obtained using HSE calculations on LDA-relaxed structures. Full HSE-relaxed structures gives +1/+2 and 0/+1 CTLs at 0.15 eV and 0.24 eV, which are in close agreement with the single-point HSE results on LDA-relaxed structures. Our results indicate that a $2 \times 2 \times 2$ k-grid is required to obtain reliable value of the formation energies and consequently CTLs for a $3 \times 3 \times 3$ Ge supercell.

Additionally, another study (Ref. 47) examined charged V_{Ge} at HSE level using a smaller 64-atoms Ge supercell and k-mesh of $2 \times 2 \times 2$. This study reported -1/0 and -2/-1 transition levels at 0.50 eV and 0.65 eV, respectively. The deviation between our results and those in Ref. 47 can be attributed to the use of less dense k-mesh ($2 \times 2 \times 2$) in Ref. 47. Our calculations yield a formation energy of 3.38 eV for a neutral V_{Ge} in a 64-atoms Ge supercell using a $2 \times 2 \times 2$ k-mesh, compared to 3.70 eV obtained with a denser $4 \times 4 \times 4$ mesh. This indicates that, for a 64-atom Ge supercell, a $2 \times 2 \times 2$ k-mesh does not converge the formation energy, and consequently the CTLs.

Another study conducted at LDA level (Ref. 45) reports the -1/0 and -2/-1 CTLs at 0.37 eV and 0.40 eV, respectively. In addition, they identify a 0/+1 transition at 0.21 eV, which is not observed in our calculations. The small energy difference between the -1/0 and -2/-1 transitions in their study is a result of ignoring spin-polarization in their calculations. The spacing between the CTLs is associated with intra-orbital repulsion, and so the spin-polarization is essential to get the correct spacing between them⁴⁸. Other factors contributing to the discrepancies between their results and ours include the use of the LDA functional, a smaller 128-atom supercell, and simulations performed exclusively at the Γ -point. The -1/0 CTL obtained using the GGA+U method in Ref. 20 is in reasonable agreement with our results, despite their use of a 64-atom Ge supercell. However, the obtained -2/-1 CTL in Ref. 20 lies close to the -1/0 CTL compared to this work.

Formation energy and charge transition level for group-V defects

Since we validated our approach by comparing our results for a V_{Ge} with previous experimental and theoretical studies, we now proceed to investigate the energetics of potential group-V impurities in Ge.

Group-V dopants are among the most common defects in Ge crystals^{17–29} and are possible contaminants in HPGe detectors during the detector manufacturing process. Figure 3a presents ΔE_F as a function of E_F for different substitutional group-V dopants in Ge. For comparison, we also included our results for V_{Ge} and Ge_i at tetrahedral site in Fig. 3a.

We infer from Fig. 3a that the formation energy of group-V defects in Ge is significantly lower than that of V_{Ge} and Ge_i . Among the group-V impurities examined in this work, P_{Ge} exhibits a much lower formation energy than N_{Ge} and its formation energy is comparable in magnitude to that of As_{Ge} and Sb_{Ge} . The formation energy of a defect is directly related to its equilibrium concentration (c_q^D) as $c_q^D = N_{sites} \exp(-\Delta E_f(D, q)/k_B T)$ ^{40,52}, where N_{sites} is the appropriate site concentration for the defect. It should be noted that the incorporation of impurities into the Ge strongly depends on their availability and ability to diffuse into the host lattice. Consequently, N, being the most abundant element in the atmosphere, is more likely to be incorporated into the crystal than other group-V impurities under typical conditions. However, assuming the similar availability of group-V dopants during the synthesis of these detectors and considering that the formation energy of P_{Ge} is significantly lower than that of N_{Ge} , V_{Ge} , and Ge_i , the concentration of P in Ge is expected to be much higher. Due to very similar formation energies, As_{Ge} and Sb_{Ge} will have similar concentration as P_{Ge} , indicating that these defects (P_{Ge} , As_{Ge} , and Sb_{Ge}) are the most prevalent defects in Ge among those considered in this study. Figure 3a also depicts that the group-V defects considered here exhibit +1/0 and -1/0 CTLs within the bandgap of Ge, indicating amphoteric behavior. The 0/+1 CTL corresponds to the donor level, where the neutral

defect donates an electron to become positively charged. Likewise, the -1/0 CTL corresponds to the acceptor level, where the neutral defect captures an electron to become negatively charged. The energetic locations of the defects depend on the type of dopant. The CTLs for P_{Ge} , As_{Ge} , and Sb_{Ge} are located near the conduction band edge, approximately at 0.64 eV and 0.75 eV for the respective 0/+1 and -1/0 transitions. N_{Ge} , however, exhibits 0/+1 charge transition at ~ 0.30 eV and -1/0 transition at ~ 0.51 eV. The ionization levels of various group-V dopants in Ge are presented in Fig. 3b.

Figure 3 also presents the results of the full HSE relaxations for N_{Ge} and P_{Ge} . As shown, the CTLs and formation energies obtained from HSE calculations on LDA-relaxed structures are in excellent agreement with those derived from the full HSE-relaxed structures. We deduce from Figure 3a and b that the group-V impurities can introduce both shallow and deep traps in Ge. These traps can impact the performance of HPGGe detectors by capturing the carriers, thereby affecting their energy resolution and hence the ability to detect traces of rare physical events in nature.

Defect complexes

Stability of defect complexes

It has been found experimentally^{18,19} and theoretically^{20,21,26,28,29} that the diffusion of group-V dopants in Ge is facilitated by Ge vacancies. A neutral Ge vacancy has a high formation energy of 3.82 eV, meaning it can only be introduced under non-equilibrium growth conditions such as ion implantation or electron irradiation^{45,50,53,54}. Once formed, Ge vacancies can interact with group-V dopants to form defect complexes, provided the defects are in close proximity. To assess their stability, we analyze the binding energies of these defect complexes. Our analysis begins with the binding energies of neutral defect complexes and is then extended to charged complexes by evaluating their binding energies as a function of E_F across the Ge bandgap, thereby providing a comprehensive understanding of their energetics.

The binding energy (E_b) of a neutral defect complex was computed using^{39,40}:

$$E_b = \Delta E_f^{\text{complex}} - \sum \Delta E_f^{\text{isolated}} \quad (4)$$

where $\Delta E_f^{\text{complex}}$ and $\Delta E_f^{\text{isolated}}$ are formation energies of a defect complex and isolated defect. The summation in Eq. (4) is over all the defects that form a complex. A positive E_b indicates repulsion between defects, thus such defect complex is not stable. In contrast, a negative E_b indicates that the defect complex is stable.

In this study, we investigated the defect complexes formed from pairs and triplets of isolated defects, as illustrated in Figs. 4 and 5. For convenience, we denote the $V_{Ge}V_{Ge}$ complex simply as VV and $P_{Ge}P_{Ge}$ complex as PP. Similarly, $P_{Ge}P_{Ge}P_{Ge}$, $P_{Ge}V_{Ge}P_{Ge}$, $P_{Ge}P_{Ge}V_{Ge}$ and $V_{Ge}P_{Ge}V_{Ge}$ complexes are denoted as PPP, PVP, PPV, and VPV, respectively. Defect complexes involving N, As, and Sb are represented using the same notation.

We begin by examining the stability of a neutral VV complex in Ge. The calculated formation energy of a neutral VV complex in this study is 6.03 eV. Our calculations yield a binding energy of -1.61 eV for the VV complex, indicating strong binding between the two vacancies upon formation. This finding is consistent with previous experimental and theoretical studies, which suggest that vacancies in Ge have a tendency to cluster and form voids^{18–21,26,28,29,55}.

Table 4 presents the computed formation and binding energies for neutral defect complexes in Ge. Our calculations indicate that, unlike NN and NNN complexes, which exhibit strong binding between N dopants, DD and DDD complexes (where D = P, As, and Sb) are not stable in Ge. This instability is reflected in their positive or nearly positive binding energies, as shown in Table 4. We further predict that vacancies can form stable defect clusters with group-V dopants, as evidenced by their negative binding energies in Table 4. This result aligns with previous experimental and theoretical studies that also suggest the formation of defect clusters in Ge^{18–21,26,28,29,55}. Additionally, our calculations reveal that N forms the most strongly bound defect complexes, although the formation energies of N-related complexes with vacancies are larger than formation energies of P, As, and Sb related defect complexes. Among the studied defect structures, DVD complexes (where D = N, P, As, and Sb) exhibit significantly stronger binding compared to DDV and VDV complexes. This suggests that group-V dopants preferentially occupy the nearest neighboring sites on either side of the vacancy when forming

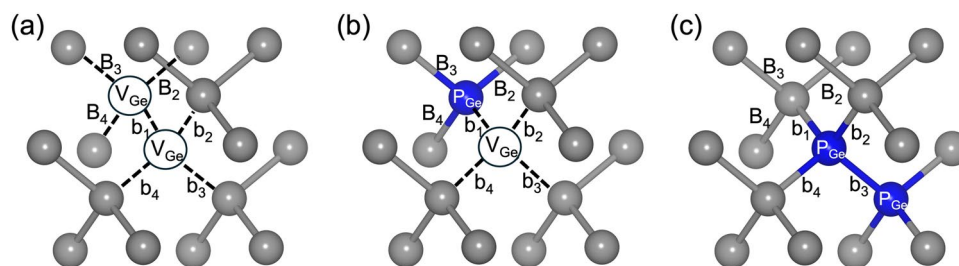


Fig. 4. Illustration of defect complexes considered in this study for complexes with two defects. (a) VV complex, (b) PV complex, and (c) PP complex. The gray and blue spheres represent Ge and Phosphorus (P) atoms, respectively.

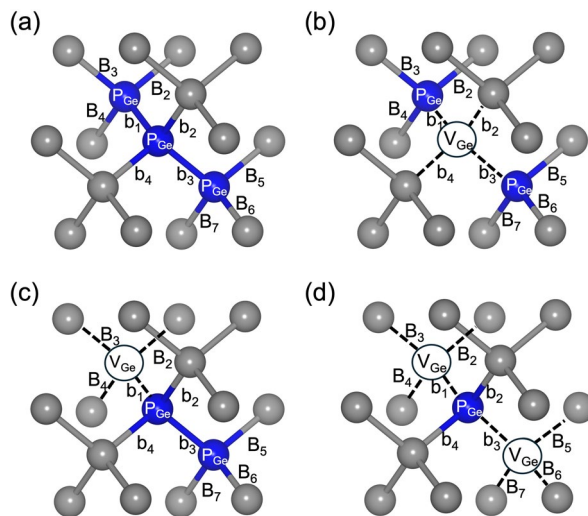


Fig. 5. Illustration of defect complexes considered in this study for complexes with three defects. (a) PPP complex, (b) PVP complex, (c) PPV complex, and (d) VPV-complex. The gray and blue spheres represent Ge and P atoms, respectively.

Dopant		DD	DV	VDV	DDD	DVD	DDV
N	ΔE_f (eV)	3.28	4.69	8.25	5.69	5.11	6.99
	E_b (eV)	-2.26	-1.90	-2.16	-2.62	-4.25	-2.37
P	ΔE_f (eV)	1.05	3.08	6.84	1.65	2.16	3.10
	E_b (eV)	-0.03	-1.28	-1.35	0.02	-2.74	-1.81
As	ΔE_f (eV)	1.38	3.06	6.69	1.92	2.18	-
	E_b (eV)	0.09	-1.40	-1.60	-0.01	-2.94	-
Sb	ΔE_f (eV)	1.91	3.14	6.39	3.25	2.43	-
	E_b (eV)	0.26	-1.51	-2.07	0.78	-3.05	-

Table 4. Calculated formation (ΔE_f) and binding (E_b) energies of neutral defect complexes at HSE06 level. D represents N, P, As, and Sb dopant.

defect complexes, a behavior that has also been observed experimentally in a previous study¹⁸. We also infer from our calculations that larger defect complexes with vacancies exhibit significantly stronger binding than the smaller ones. For instance, the binding energy for a PVP complex is -2.74 eV, compared to the -1.28 eV for a PV complex. We also find that vacancy in Ge lower its formation energy by forming defect complexes with P, As, and Sb. For example, the formation energy of a PVP (~ 2.16 eV) complex is lower than a PV (~ 3.08 eV) complex, which in turn is lower than the formation energy an isolated Ge vacancy (~ 3.82 eV). Such significant reduction in formation energy upon clustering, along with the strong binding of these defect complexes, suggests that larger complexes are energetically more favorable in Ge, provided the defects diffuse and come into close proximity. Our calculations also reveal that AsAsV and SbSbV complexes relax to the respective AsVAs and SbSbV complexes, respectively, indicating a preference for these rearranged structures. The computed binding energies for defect complexes are in good qualitative agreement with previous studies conducted at GGA level^{25,27}. However, in this work, we examined the stability of these complexes using a more accurate hybrid functional approach.

Defects can exist in different charge states within the bandgap, and their stability is strongly influenced by the electron chemical potential (E_F). Therefore, we next evaluate binding energy (E_b) as a function of E_F within the Ge bandgap. For our analysis, we focus on defect complexes of the XV and XVX types. Since the results for P, As, and Sb are very similar (see Table 4), particularly when a vacancy is involved, we only computed and analyzed the binding energies of various phosphorus-related complexes, including PPP, PPV, VPV, and PVP, as a function of E_F . The results of these calculations are presented in Figs. S2–S4.

To determine E_b as a function of E_F , we start by analyzing the simplest XV-type complexes and then extend the approach to larger defect complexes. As an example, let us consider the formation of a dopant–vacancy complex through the following reaction as in Ref. 56

$$D_{Ge}^q + V_{Ge}^{q'} - (q'' - (q' + q))e^{-\frac{E_b}{kT}} = (D_{Ge}V_{Ge})^{q''}, \quad (5)$$

where D represents a dopant atom (N, P, As, or Sb), while q , q' , and q'' denote the charge states of the dopant, vacancy, and complex, respectively. e^- is an electron charge. The binding energy of a defect-complex can be expressed in terms of the formation energies of its constituents as

$$E_b = \Delta E_f[(D_{Ge}V_{Ge})^{q''}] - \Delta E_f[D_{Ge}^q] - \Delta E_f[V_{Ge}^{q'}]. \quad (6)$$

Because the slope of ΔE_f with respect to E_F corresponds to the charge state of the defect, and each segment between charge transitions is linear in E_F , E_b is piecewise linear, with the slope given by

$$\frac{dE_b}{dE_F} = q'' - (q' + q). \quad (7)$$

This slope is zero only if the complex forms without exchanging electrons with the electron reservoir. A negative value ($q'' - q' - q < 0$) means that the defect-complex formation happens by electrons capture from the electron reservoir⁵⁶. In contrast, a positive value ($q'' - q' - q > 0$) signifies that electrons are instead released into the electron reservoir as the complex forms⁵⁶.

Figure S2 presents E_b as a function of E_F for the simplest defect complexes of type XV ($X = N, P, As, Sb$) formed from isolated X ($X = N, P, As, Sb$) and V_{Ge} defects. For clarity, the corresponding formation energies as a function of E_F are also included. Kinks in the E_b curves occur at the CTLs, i.e. whenever the charge state of a defect changes in the formation energy plot. Across the entire range of E_F within the bandgap, the binding energies remain negative, indicating that these complexes are strongly bound. In particular, for P-, As-, and Sb-based complexes, E_b becomes increasingly negative as E_F moves from VBM toward the CBM, suggesting that the binding increases, except in the nearest vicinity of the CBM. For the NV-complex, the binding energy decreases (becomes more negative) as the Fermi level moves away from the VBM and subsequently increases as it approaches the CBM. The calculated binding energy spans from -1.60 eV to -1.96 eV for NV, and from approximately -0.63 eV to -1.32 eV for PV complex; the binding energy results for AsV, and SbV complexes are very similar to PV complex. As shown in Fig. S2, there is no region within the bandgap where the neutral charge states of the complex and the isolated defects overlap. Hence, evaluating E_b as a function of E_F is essential to capture full picture of the defect energetics.

Equations (5) and (6) can also be generalized to the larger defect complexes. For the larger XVX complexes ($X = N, P, As, Sb$), our results indicate the same overall trend as for the simplest defect complexes, which can be seen in Fig. S3. However, the larger complexes show much stronger binding, as reflected by their more negative E_b values. Our calculations further reveal that the PPP complex (see Fig. S4) exhibits positive binding energy throughout the entire E_F range, indicating that it is unstable. By contrast, other complexes such as VPV and PPV are bound within the bandgap, though their binding is weaker compared to the PVP complexes.

Similar to Ge vacancies and other group-V defects, the formation of defect complexes in Ge alters its local structural properties. The structural modifications, specifically in terms of Ge-defect and defect-defect bond lengths for the simplest defect complexes, are summarized in Table S1. Our calculations indicate that structural changes near the defect site are more pronounced for N-related defect complexes compared to those involving P, As, and Sb. This difference arises from variations in atomic size and electronegativity among the group-V dopants studied here. However, beyond the immediate vicinity of the defect complex, no significant structural changes are observed.

Formation energy and charge transition level for defect complexes

Next, we examine the energetics of the simplest defect complexes formed by clustering of a single vacancy with a single group-V dopant in Ge. Figure 6 presents ΔE_f as a function of E_F for these defect clusters. Our calculations reveal that, similar to V_{Ge} , defect complexes primarily exist in the 0, -1, and -2 charge states within the bandgap of Ge. The formation energy of an NV complex in these charge states is significantly higher than that of PV, AsV, and SbV complexes. For instance, the formation energy of a neutral NV complex is approximately 4.69 eV, whereas the formation energy for PV, AsV, and SbV complexes is around 3.10 eV. Due to their similar formation energies across different charge states, PV, AsV, and SbV complexes are expected to have comparable concentrations in Ge. Furthermore, Figure 6 indicates that defect-vacancy complexes are more likely to be in a doubly negative charge state under n-type doping conditions, consistent with a previous theoretical study performed using the GGA+U method²⁰.

Figure 6a and b illustrates that these defect complexes exhibit -1/0 and -2/-1 CTLs within the electronic bandgap of Ge. Similar to the formation energies shown in Fig. 6, our calculations indicate that PV, AsV, and SbV complexes have nearly identical CTLs. The -1/0 and -2/-1 transitions for these complexes are located at approximately 0.17 eV and 0.35 eV, respectively. This suggests that their CTLs are very close to the corresponding ionization levels of V_{Ge} . Notably, the SbV complex exhibits an additional 0/+1 CTL near the valence band edge at 0.015 eV. However, this defect level is relatively shallow and less detrimental compared to the deeper traps associated with SbV cluster. Unlike PV, AsV, and SbV complexes, the -2/-1 CTL for the NV complex is slightly deeper, located at 0.42 eV. However, its -1/0 CTL (0.17 eV) is similar to other defect complexes considered in this study.

Figure 6 also confirms that, like V_{Ge} , these defect complexes behave as multi-level acceptors, despite being composed of donor-type dopants.

To assess the reliability of the CTLs obtained from single-point HSE calculations on LDA-relaxed structures, we also carried out full HSE relaxations for the NV and PV complexes. The results, shown by the dotted black (PV) and dotted steel blue (NV) lines in Fig. 6a, indicate that the full HSE-relaxed structures yield -1/0 and -2/-1 CTLs at 0.23 eV and 0.41 eV for the NV complex. The corresponding values for the PV complex are at 0.22 eV

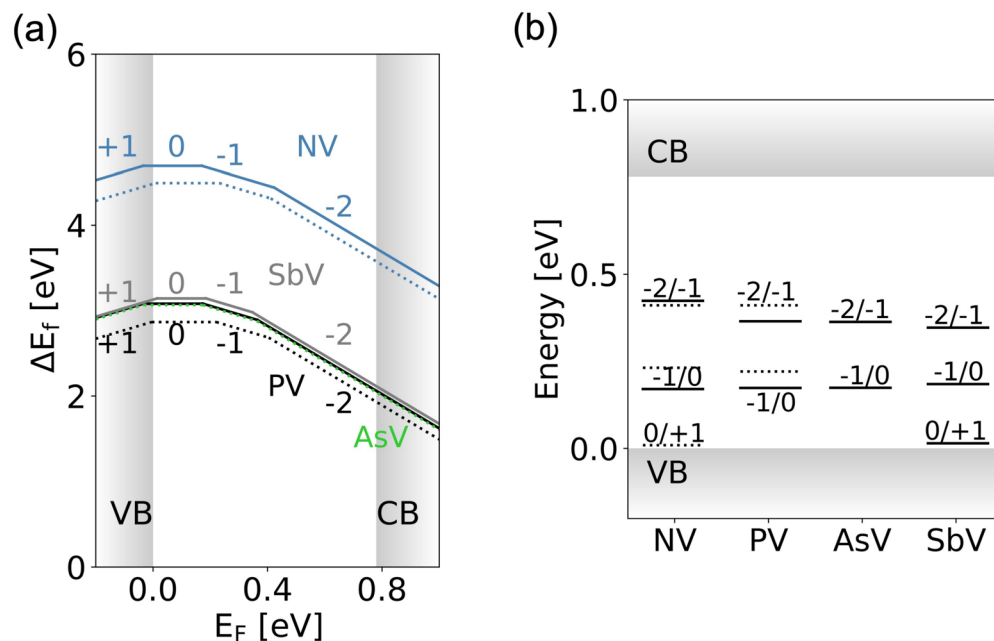


Fig. 6. (a) Formation energy (ΔE_F) of defect complexes of the type XV ($X = N, P, As, Sb$) as a function of the electron chemical potential (E_F). (b) Corresponding charge transition levels (CTLs) for the defect complexes shown in (a). In both panels, the dotted black (PV) and steel blue (NV) lines represent the corresponding results obtained using full HSE-relaxed structures. The shaded regions denote the valence band (VB) and conduction band (CB).

Transitions	NV	PV	AsV	SbV
0/+1	-	-	-	0.015
-1/0	0.17	0.17 (0.28) ^a	0.17 (0.26) ^a	0.18 (0.17) ^a
-2/-1	0.42	0.37 (0.52) ^a	0.36 (0.47) ^a	0.35 (0.18) ^a

Table 5. Calculated charge transition levels for XV ($X = N, P, As, Sb$) defect complexes. ^aRef. 20. The values in the parenthesis are obtained using GGA+U method in Ref. 20.

and 0.40 eV for the -1/0 and -2/-1 transitions. These results demonstrate that CTLs obtained from single-point HSE calculations on LDA-relaxed structures (see Table 5) are in excellent agreement with those yielded from full HSE-relaxed structures.

Table 5 summarizes the computed CTLs for these defect complexes and compares them with previously reported theoretical values. The discrepancies between the transition levels in the two studies are likely due to differences in supercell size and computational method (GGA+U) used in Ref. 20.

However, XV ($X = N, P, As, Sb$) complexes represent the simplest vacancy-dopant complex, and it is highly likely that the defects cluster into larger defect complexes in HPGe detectors. To examine the impact of such large complexes, we extend our analysis to investigate CTLs associated with complexes of type XVX ($X = N, P, As, Sb$). Figure 7 presents ΔE_F as a function of E_F for XVX complexes. Similar to XV complexes, XVX defect complexes are stable in the 0, -1, and -2 charge states within the bandgap of Ge, and generally introduce deep traps away from the band edges. Among them, the N-related complex exhibits a significantly higher formation energy compared to the other defect complexes shown in Fig. 7. The computed -1/0 and -2/-1 CTLs for the NVN complex are at 0.29 eV and 0.49 eV from the VBM. Calculations reveal that the PVP and AsVAs complexes not only possess nearly identical formation energies but also produce CTLs that lie extremely close to each other, with the -1/0 and -2/-1 transitions at approximately 0.22 eV and 0.41 eV. On the other hand, SbVSb complex forms -1/0 and -2/-1 CTLs at 0.18 eV and 0.31 eV, respectively. These results are summarized in Table 6. Our calculations, thus, show that XV and XVX ($X = P, As, Sb$) complexes in Ge exhibit CTLs very similar to those of a V_{Ge} . Furthermore, like a V_{Ge} and simplest defect complexes, the XVX complexes introduce deep traps in Ge.

We also performed fully relaxed HSE calculations for the PVP complex. As shown by the black dotted lines in Fig. 7a and b, the results are in good agreement with single-point HSE calculations on the LDA-relaxed structures. The -1/0 and -2/-1 transitions differ by no more than 0.08 eV between the two approach (see Table 6), confirming their consistency.

In this work, we further compute and analyze CTLs for different phosphorus-related complexes, namely PPP, PPV, and VPV. Our calculations indicate that the PPP complex has CTLs comparable to those of a single

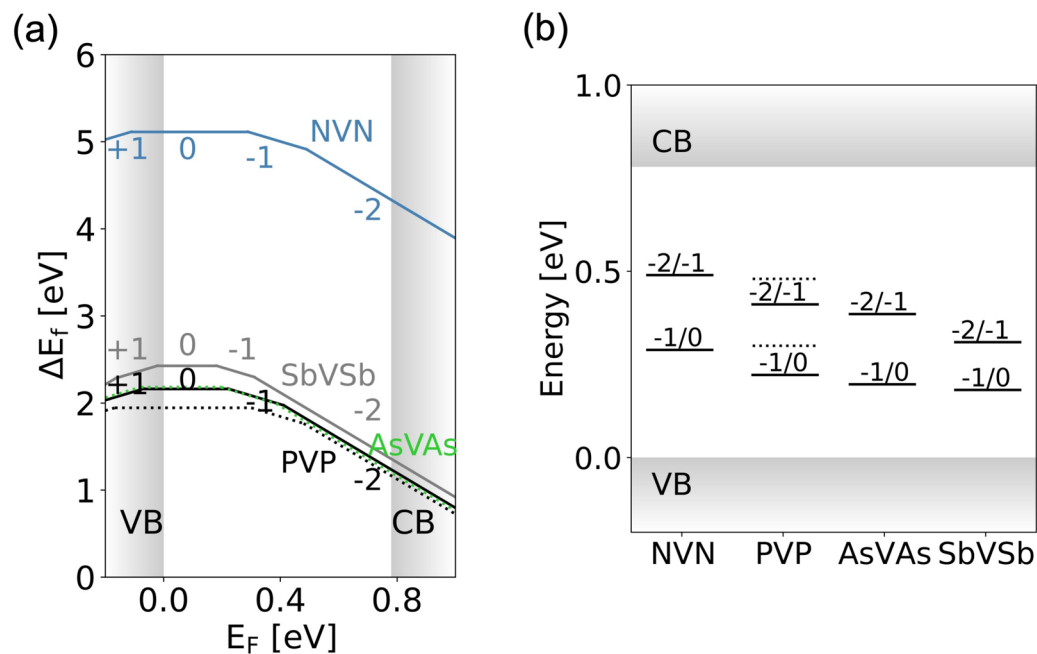


Fig. 7. (a) Formation energy (ΔE_f) of defect complexes of the type XVX (X = N, P, As, Sb) as a function of the electron chemical potential (E_f). (b) Corresponding charge transition levels (CTLs) for the defect complexes shown in (a). In both panels, the dotted black lines represent results for PVP complex obtained using full HSE-relaxed structures. The shaded regions denote the valence band (VB) and conduction band (CB).

Transitions	NVN	PVP	AsVAs	SbVSb
-1/0	0.29	0.22 (0.30)	0.20	0.18
-2/-1	0.49	0.41 (0.48)	0.39	0.31

Table 6. Calculated charge transition level (eV) for XVX (X = N, P, As, Sb) defect complexes. The values in parenthesis for PVP complex are obtained using full HSE-relaxed structures.

P dopant in Ge, although its formation energy is substantially higher. Specifically, the PPP complex forms 0/+1 and -1/0 CTLs at 0.65 eV and 0.78 eV, respectively. However, it may be noted that PPP complex does not bind and may not be stable in Ge. In contrast, the VPV complex has a much larger formation energy than the other phosphorus-related complexes and introduces -1/0 and -2/-1 CTLs at 0.09 eV and 0.24 eV in Ge. The PPV complex, while exhibiting slightly higher formation energy than the PVP complex, induces -1/0 and -2/-1 CTLs at 0.24 eV and 0.39 eV, along with an additional 0/+1 transition level at 0.03 eV. The results of these calculations have been presented in Fig. S5.

Based on this study, we infer that although the group-V dopants in Ge generally form shallow traps (except N), their complexes with vacancies give rise to deep traps in Ge. Such traps are expected to degrade the performance of HPGe detectors by capturing carriers generated through the interaction of incoming radiation with Ge atoms, thereby reducing the number of carriers collected at the electrodes.

Shallow traps, located close to the band edges, allow carriers to undergo continuous trapping and de-trapping phenomena due to thermal agitation $\sim k_B T$, where k_B is the Boltzmann constant and T is the absolute temperature. While continuous trapping and de-trapping reduces the carrier mobility, it does not result in permanent carrier loss. In contrast, deep traps, located away from the band edges, captures carriers for a long time, resulting permanent charge loss, lowering charge collection efficiency and degrading the performance HPGe detectors.

The deep traps formed due to vacancy-impurity complexes are detrimental for HPGe detectors, which require minimal defect concentration and efficient charge collection at the electrodes to achieve excellent energy resolution. It may be noted that a small concentration of defects in HPGe detectors can introduce significant charge carrier loss, reduce detector sensitivity, and limit the ability of these detectors to detect rare physical events, such as $0\nu\beta\beta$. Therefore, controlling the introduction of vacancies and group-V impurities during synthesis is vital to suppress the formation of detrimental defect complexes and to ensure the optimal performance of Ge-based radiation detectors.

Conclusions

In summary, we employed a hybrid functional within DFT to investigate group-V defects and their complexes in Ge. Our calculations indicate that group-V dopants are easily accommodated in Ge, and except N, they, in general, induce shallow traps just below the conduction band edge. Vacancy and interstitial of Ge, on the other hand, have relatively high formation energies and give rise to deeper traps. We also find that group-V defects strongly bind with Ge vacancies, with larger complexes binding more strongly and exhibiting lower formation energies than smaller ones. For example, the formation energy of a PVP complex is lower than that of a PV complex by 0.92 eV, which, in turn, is lower than the formation energy of a vacancy by 0.74 eV in Ge. This reveals a clear preference for defect clustering, provided the defects diffuse and encounter each other in their proximity. Crucially, these impurity–vacancy complexes introduce deep traps in Ge, which cause charge trapping in HPGe detectors and degrade energy resolution. This work is expected to advance our understanding of group-V defect behavior in Ge and aid in developing necessary mitigation strategies to suppress such defects during the fabrication process of HPGe detectors, thereby enhancing their performance in detecting rare physical events, such as $0\nu\beta\beta$.

Data availability

Data is provided within the manuscript or supplementary information files.

Received: 22 May 2025; Accepted: 17 October 2025

Published online: 11 December 2025

References

1. Abrosimov, N. et al. Technology development of high purity germanium crystals for radiation detectors. *J. Cryst. Growth* **532**, 125396 (2020).
2. Abgrall, N. et al. The Majorana demonstrator neutrinoless double-beta decay experiment. *Adv. High Energy Phys.* **2014**, 365432 (2014).
3. Aalseth, C. E. et al. Search for neutrinoless double- β decay in ge 76 with the Majorana demonstrator. *Phys. Rev. Lett.* **120**, 132502 (2018).
4. An, F. et al. Observation of electron-antineutrino disappearance at Daya Bay. *Phys. Rev. Lett.* **108**, 171803 (2012).
5. Ahmad, Q. R. et al. Direct evidence for neutrino flavor transformation from neutral-current interactions in the Sudbury Neutrino Observatory. *Phys. Rev. Lett.* **89**, 011301 (2002).
6. Yang, J. et al. A feasibility study of multi-electrode high-purity germanium detector for ^{76}Ge neutrinoless double beta decay searching. *JINST* **18**, P05025 (2023).
7. Fukuda, Y. et al. Evidence for oscillation of atmospheric neutrinos. *Phys. Rev. Lett.* **81**, 1562 (1998).
8. Agostini, M. et al. Search of neutrinoless double beta decay with the GERDA experiment. *Nucl. Part. Phys. Proc.* **273**, 1876–1882 (2016).
9. Heider, M. B. et al. Performance of bare high-purity germanium detectors in liquid argon for the GERDA experiment. *IEEE Nucl. Sci. Symp. Conf. Record.* **2008**, 3513–3516 (2008).
10. Abgrall, N. et al. The large enriched germanium experiment for neutrinoless double beta decay (LEGEND). In AIP Conference Proc. (2017).
11. Dai, W. et al. Search for neutrinoless double-beta decay of Ge 76 with a natural broad energy germanium detector. *Phys. Rev. D* **106**, 032012 (2022).
12. Van Sande, M., Van Goethem, L., De Laet, L. & Guislain, H. Dislocations in high-purity germanium and its relation to γ -ray detector performance. *Appl. Phys. A* **40**, 257–261 (1986).
13. Agostini, M. et al. Characterization of 30 ^{76}Ge enriched Broad Energy Ge detectors for GERDA Phase II. *Eur. Phys. J. C* **79**, 1–24 (2019).
14. Agostini, M. et al. Limits on uranium and thorium bulk content in GERDA Phase I detectors. *Astropart. Phys.* **91**, 15–21 (2017).
15. Ferella, F. et al. Enriched high purity germanium detectors for the LEGEND-200 experiment: Purification and characterization by quadrupole and high resolution inductively coupled plasma mass spectrometry (ICP-MS). *Appl. Radiat. Isot.* **200**, 110904 (2023).
16. Mei, D. et al. Impact of charge trapping on the energy resolution of Ge detectors for rare-event physics searches. *J. Phys. G Nucl. Part.* **47**, 105106 (2020).
17. Chroneos, A. & Bracht, H. Diffusion of n-type dopants in germanium. *Appl. Phys. Rev.* **1**, 011301 (2014).
18. Brotzmann, S. et al. Diffusion and defect reactions between donors, C, and vacancies in Ge I. Experimental results. *Phys. Rev. B* **77**, 235207 (2008).
19. Brotzmann, S. & Bracht, H. Intrinsic and extrinsic diffusion of phosphorus, arsenic, and antimony in germanium. *J. Appl. Phys.* **103**, 033508 (2008).
20. Tahini, H., Chroneos, A., Grimes, R., Schwingenschlögl, U. & Bracht, H. Diffusion of E centers in germanium predicted using GGA+ U approach. *Appl. Phys. Lett.* **99**, 072112 (2011).
21. Chroneos, A., Grimes, R., Uberuaga, B. P. & Bracht, H. Diffusion and defect reactions between donors, C, and vacancies in Ge. II. Atomistic calculations of related complexes. *Phys. Rev. B* **77**, 235208 (2008).
22. Markevich, V., Peaker, A., Litvinov, V., Emtsev, V. & Murin, L. Electronic properties of antimony-vacancy complex in Ge crystals. *J. Appl. Phys.* **95**, 4078–4083 (2004).
23. Markevich, V. et al. Vacancy-group-V-impurity atom pairs in Ge crystals doped with P, As, Sb, and Bi. *Phys. Rev. B* **70**, 235213 (2004).
24. Lindberg, C. et al. The antimony-vacancy defect in p-type germanium. *Appl. Phys. Lett.* **87**, 172103 (2005).
25. Chroneos, A. Dopant-vacancy cluster formation in germanium. *J. Appl. Phys.* **107**, 076102 (2010).
26. Chroneos, A., Bracht, H., Grimes, R. & Uberuaga, B. P. Vacancy-mediated dopant diffusion activation enthalpies for germanium. *Appl. Phys. Lett.* **92**, 172103 (2008).
27. Chroneos, A. Effect of germanium substrate loss and nitrogen on dopant diffusion in germanium. *J. Appl. Phys.* **105**, 056101 (2009).
28. Chroneos, A., Bracht, H., Grimes, R. & Uberuaga, B. P. Phosphorous clustering in germanium-rich silicon germanium. *Mater. Sci. Eng. B* **154**, 72–75 (2008).
29. Chroneos, A., Grimes, R., Uberuaga, B. P., Brotzmann, S. & Bracht, H. Vacancy-arsenic clusters in germanium. *Appl. Phys. Lett.* **91**, 192106 (2007).
30. Kresse, G. & Furthmüller, J. Efficient iterative schemes for ab initio total-energy calculations using a plane-wave basis set. *Phys. Rev. B* **54**, 11169 (1996).

31. Kresse, G. & Furthmüller, J. Efficiency of ab-initio total energy calculations for metals and semiconductors using a plane-wave basis set. *Comput. Mater. Sci.* **6**, 15–50 (1996).
32. Arrigoni, M. & Madsen, G. K. Spinney: Post-processing of first-principles calculations of point defects in semiconductors with Python. *Comput. Phys. Commun.* **264**, 107946 (2021).
33. Kresse, G. & Joubert, D. From ultrasoft pseudopotentials to the projector augmented-wave method. *Phys. Rev. B* **59**, 1758 (1999).
34. Blöchl, P. E. Projector augmented-wave method. *Phys. Rev. B* **50**, 17953 (1994).
35. Heyd, J. & Scuseria, G. E. Efficient hybrid density functional calculations in solids: Assessment of the Heyd-Scuseria-Ernzerhof screened Coulomb hybrid functional. *J. Chem. Phys.* **121**, 1187–1192 (2004).
36. Heyd, J., Scuseria, G. E. & Ernzerhof, M. Hybrid functionals based on a screened Coulomb potential. *J. Chem. Phys.* **118**, 8207–8215 (2003).
37. Monkhorst, H. J. & Pack, J. D. Special points for Brillouin-zone integrations. *Phys. Rev. B* **13**, 5188 (1976).
38. Kumagai, Y. & Oba, F. Electrostatics-based finite-size corrections for first-principles point defect calculations. *Phys. Rev. B* **89**, 195205 (2014).
39. Van de Walle, C. G. & Neugebauer, J. First-principles calculations for defects and impurities: Applications to III-nitrides. *J. Appl. Phys.* **95**, 3851–3879 (2004).
40. Freysoldt, C. et al. First-principles calculations for point defects in solids. *Rev. Mod. Phys.* **86**, 253–305 (2014).
41. Kittel, C. & McEuen, P. *Introduction to Solid State Physics* (Wiley, 2018).
42. Smakula, A., Kalnajs, J. & Sils, V. Densities and imperfections of single crystals. *Phys. Rev.* **99**, 1747 (1955).
43. Morin, F. & Maita, J. P. Conductivity and Hall effect in the intrinsic range of germanium. *Phys. Rev.* **94**, 1525 (1954).
44. Sze, S. M., Li, Y. & Ng, K. K. *Physics of Semiconductor Devices* (Wiley, 2021).
45. Fazzio, A., Janotti, A., da Silva, A. J. & Mota, R. Microscopic picture of the single vacancy in germanium. *Phys. Rev. B* **61**, R2401 (2000).
46. Śpiewak, P., Vanhellefont, J., Sueoka, K., Kurzydłowski, K. & Romandic, I. First principles calculations of the formation energy and deep levels associated with the neutral and charged vacancy in germanium. *J. Appl. Phys.* **103**, 086103 (2008).
47. Śpiewak, P., Vanhellefont, J. & Kurzydłowski, K. Improved calculation of vacancy properties in Ge using the Heyd-Scuseria-Ernzerhof range-separated hybrid functional. *J. Appl. Phys.* **110**, 063534 (2011).
48. Weber, J., Janotti, A. & Van de Walle, C. Dangling bonds and vacancies in germanium. *Phys. Rev. B* **87**, 035203 (2013).
49. Ramprasad, R., Zhu, H., Rinke, P. & Scheffler, M. New perspective on formation energies and energy levels of point defects in nonmetals. *Phys. Rev. Lett.* **108**, 066404 (2012).
50. Haesslein, H., Sielemann, R. & Zistl, C. Vacancies and self-interstitials in germanium observed by perturbed angular correlation spectroscopy. *Phys. Rev. Lett.* **80**, 2626 (1998).
51. Zistl, C. et al. DLTS combined with perturbed angular correlation (PAC) on radioactive ¹¹¹In atoms in Ge. *Mater. Sci. Forum* **258**, 53–58 (1997).
52. Van de Walle, C. G., Laks, D., Neumark, G. & Pantelides, S. First-principles calculations of solubilities and doping limits: Li, Na, and N in ZnSe. *Phys. Rev. B* **47**, 9425 (1993).
53. Feuser, U. et al. Vacancy-acceptor complexes in germanium produced by ion implantation. *Nucl. Instrum. Methods Phys. Res. B* **59**, 1049–1052 (1991).
54. Potsidi, M. et al. Theoretical investigation of nitrogen-vacancy defects in silicon. *AIP Adv.* **12**, 025112 (2022).
55. Gradwohl, K.-P. *Growth and Defect Investigation of High-purity Germanium Crystals for Radiation Detector Applications* (Humboldt Universitaet zu Berlin (Germany), 2021).
56. Tan, A. M. Z., Freysoldt, C. & Hennig, R. G. First-principles investigation of charged dopants and dopant-vacancy defect complexes in monolayer MoS₂. *Phys. Rev. Mater.* **4**, 114002 (2020).

Author contributions

S.A.: Methodology, Investigation, Data curation, and Writing—original draft. E.B.: Methodology, Investigation, and Writing—review, editing. G.W.: Methodology, Funding acquisition, and Writing—review, editing.

Funding

The authors gratefully acknowledge the funding for this work from the Laboratory Directed Research and Development program at Los Alamos National Laboratory (LANL) under project 20230047DR. Los Alamos National Laboratory is operated by Triad National Security, LLC, for the National Nuclear Security Administration of the U.S. Department of Energy (contract no. 89233218CNA000001). This research also utilizes LANL institutional computer—chicoma.

Declarations

Competing interests

The authors declare no competing interests.

Additional information

Supplementary Information The online version contains supplementary material available at <https://doi.org/10.1038/s41598-025-25057-6>.

Correspondence and requests for materials should be addressed to S.A. or G.W.

Reprints and permissions information is available at www.nature.com/reprints.

Publisher's note Springer Nature remains neutral with regard to jurisdictional claims in published maps and institutional affiliations.

Open Access This article is licensed under a Creative Commons Attribution-NonCommercial-NoDerivatives 4.0 International License, which permits any non-commercial use, sharing, distribution and reproduction in any medium or format, as long as you give appropriate credit to the original author(s) and the source, provide a link to the Creative Commons licence, and indicate if you modified the licensed material. You do not have permission under this licence to share adapted material derived from this article or parts of it. The images or other third party material in this article are included in the article's Creative Commons licence, unless indicated otherwise in a credit line to the material. If material is not included in the article's Creative Commons licence and your intended use is not permitted by statutory regulation or exceeds the permitted use, you will need to obtain permission directly from the copyright holder. To view a copy of this licence, visit <http://creativecommons.org/licenses/by-nc-nd/4.0/>.

© The Author(s) 2025